Evaluating the impact of low-frequency sensitivity difference of LIGO detectors on GW231123 Interim Report 1

Krzysztof Król and Mentor: Sophie Bini

ABSTRACT

GW231123 is a short duration gravitational wave signal, consistent with a binary black hole merger with a total mass of 190-265 $M_\odot$. It is the most massive binary black hole confidently observed to date. Both components are highly spinning and likely have masses in the mass gap caused by pair-instability supernova processes. The event is challenging to analyze because of its short duration and limited accuracy of waveform models for such a system. Additionally, 2 sigma differences between median total mass and median spin precession arise when parameter estimation is performed using LIGO Hanford-only and LIGO Livingston-only data, raising concerns about the presence of spurious transient noise overlapping with the GW signal. In this project, we will perform the parameter estimation of GW231123 to quantify these differences. Later, we will perform injection simulations to investigate whether the differences between the parameter estimation results can be explained by fluctuations of Gaussian noise, the difference in low-frequency sensitivity of the two LIGO detectors, or if they are related to transient noise.

1. INTRODUCTION

GW231123 is a transient gravitational wave (GW) event observed on 23 November 2023 by the two Advanced LIGO detectors (Virgo was offline at the time of detection). The signal is consistent with the coalescence of a binary black hole system with total mass of between 190-265 $M_\odot$, which makes it the most massive merger observed to date with high confidence (LVK Collaboration 2025, in preparation).

GW231123 might have very important astrophysical implications. Due to pair-instability supernova process (Farmer et al. 2019), it is believed that black holes with masses between 60 $M_\odot$ and 130 $M_\odot$ cannot form as a result of standard stellar collapse. In the case of the previous most-massive merger, GW190521 (Abbott et al. 2020a,b), the primary black hole is believed to lie in the mass gap. In the case of GW231123 the primary is within or above the mass gap produced by the pair-instability supernova process, while the secondary is within the mass gap with a probability of 83%. Further, GW231123 is the second event (after GW190521) observed that produced a remnant which would be classified as an intermediate mass black hole (a black hole with mass between $10^2 M_\odot$ and $10^5 M_\odot$).

Inferring the properties of the source of this exceptional event is particularly challenging due to its high mass. Its signal's frequency is noticeably lower than other events, peaking at close to 50 Hz. The event is also much shorter, with only a few observable cycles before merger and the entire event being shorter than 0.2 seconds.

Following parameter estimation (PE), differences between LIGO Livingston-only and LIGO Hanford-only results were noticed. In particular, the median total mass and the median spin precession differ by 2 sigma. We aim to quantify these differences and investigate their possible sources.

2. OBJECTIVES

First, we will attempt to perform PE for GW231123 and verify agreement with results that will be included in the GWTC-4 LVK catalog. Then we will repeat the process for LIGO Livingston-only and LIGO Hanford-only data, after which we hope to identify parameters that differ the most across the two detectors. Afterwards, we want to investigate one possible source of those differences – the difference in amplitude spectral density (ASD) between LIGO Livingston and LIGO Hanford, by performing an injection study.

3. METHODS

3.1. *Binary black hole coalescence parameters*

The main difficulty in parameter estimation from binary black hole GW signal comes from the multidimensionality of the data. There are 15 total parameters that describe a binary black hole waveform, namely:

- masses of the two black holes m_1 and m_2 ,
- spins $\vec{\chi_1}$ and $\vec{\chi_2}$, expressed by the dimensionless spin vector $\vec{\chi_i} = \vec{S_i}c/(Gm_i^2)$ $(0 \leq |\vec{\chi_i}| < 1)$, where S_i is the angular moment of black hole,
- luminosity distance D_L,
- inclination angle ι (angle between observer's line of sight and orbital plane of the system),

- coalescence time t_0 and phase ϕ_0,
- polarization angle ψ,
- source sky position θ and ϕ.

Due to the possibility of more precise measurement, often, instead of directly estimating the two masses, the chirp mass $\mathcal{M}$ is used, which is defined as

$$\mathcal{M} = \frac{(m_1 m_2)^{3/5}}{(m_1 + m_2)^{1/5}}$$

for $m_1 > m_2$. Beyond that, in describing the system as a whole, it is often useful to introduce the spin parameters $\chi_{\rm eff}$ and $\chi_{\rm p}$, which are the effective aligned spin and effective precessing spin, as they can be inferred more accurately than the individual spins. They are defined as (Ng et al. 2018; Thomas et al. 2021):

$$\chi_{\rm eff} = \frac{\vec{S_1}/m_1 + \vec{S_2}/m_2}{m_1 + m_2} \cdot \vec{L}$$

and

$$\chi_{\rm p} = \frac{\max(A_1|\vec{S_1}|,\ A_2|\vec{S_2}|)}{A_1 m_1^2},$$

where $A_1 = 2 + 3/2q$ and $A_2 = 2 + 3q/2$. $\chi_{\rm eff}$ is bounded by $[-1, 1]$ and $\chi_{\rm p}$ by $[0, 1]$ to avoid naked singularities. Furthermore, $\chi_{\rm eff}$ is a constant of motion up to at least the second post-Newtonian order (Racine 2008; Blanchet 2014).

3.2. *Bayesian statistics*

To infer the properties of GW signals, we use Bayesian statistics. Bayesian statistics is based on an interpretation of probability, where, unlike in the frequentist approach, probability expresses a degree of belief. It is achieved by combining prior knowledge with new data to compute new probabilities ("posterior") according to Bayes' theorem:

$$P(A|B) = \frac{P(B|A)P(A)}{P(B)}$$

where $P(A)$ is the prior probability, $P(B)$ is the probability of new observations, $P(B|A)$ the likelihood, and $P(A|B)$ the posterior probability. In the context of parameter estimation, Bayes' theorem can be rewritten as

$$p(\theta|d) = \frac{L(d|\theta)\pi(\theta)}{\int L(d|\theta)\pi(\theta)\,\mathrm{d}\theta}$$

where observations are denoted by d, unknown parameters are denoted by θ, L is the likelihood function and π is the prior probability density function (Christensen & Meyer 2022). The denominator serves as a normalization constant.

3.3. *Data preprocessing and sampling settings*

We perform our PE using whitened, bandpassed data. A glitch in LIGO Hanford occurred 1.7-1.1 s before the event in a frequency range between 15-30 Hz. It was modeled along with the waveform using BayesWave (Cornish & Littenberg 2015; Cornish et al. 2021; Chatziioannou et al. 2021). Another glitch occurred in LIGO Livingston 3.0-2.0 s in a frequency range between 10-20 Hz. This glitch, due to low frequency and the extended time between the event and the glitch, was not removed from the LIGO Livingston strain data.

We perform PE using `bilby` (Ashton et al. 2019), a Python library for GW-related Bayesian inference. It allows one to perform parameter estimation for a GW signal using nested sampling (Ashton et al. 2019). We are using the same PSD, likelihood, and sampler settings as for the GWTC-4 catalog.

3.4. *Comparing posterior distributions*

To understand the differences between posterior distributions resulting from different PE runs, we will both be examining the corner plots containing relevant parameters and trying to quantify them. To do the latter, we will use the Jensen-Shannon (JS) divergence between two posterior distributions Q_1 and Q_2, which is defined as:

$$JS(Q_1||Q_2) = \frac{1}{2}D(Q_1||M) + \frac{1}{2}D(Q_2||M),$$

where $M = \frac{1}{2}(P+Q)$ is a mixture distribution of Q_1 and Q_2, and $D(Q_1||Q_2)$ is the Kullback-Leibler divergence defined as:

$$D(Q_1||Q_2) = \sum_{x \in X} P(x) \log \frac{Q_1(x)}{Q_2(x)}.$$

The JS divergence is a real number in the range $[0, 1]$ for discrete probability distributions (as is the case for numerically calculated posterior distributions), where $JS = 0$ means the distributions are identical.

4. SOURCE PROPERTIES OF GW231123

4.1. *Waveform approximant choice and ASD difference quantification*

The GW231123 paper (LVK Collaboration 2025, in preparation) found that the NRSur7dq4 (Varma et al. 2019) waveform model is on average more accurate than every other waveform model tested (IMRPhenomXPHM, IMRPhenomXO4a, IMRPhenomTPHM, SEOB-NRv5PHM) for events similar to GW231123. We first attempted using NRSur7dq4 to perform PE and for further studies, but

quickly discovered that its computational cost along with current LIGO Data Grid's load significantly slowed us down. We therefore decided to use IMRPhenomXPHM (Pratten et al. 2021), which offers close to 5× computational speedup.

In making this decision we inspected results from PE using both models and discovered a significant difference in the average modeled waveform's ASD between the two models. We plot this in Figure 1 and Figure 2 for NRSur7dq4 and IMRPhenomXPHM, respectively. Significant differences in LIGO Hanford and LIGO Livingston's sensitivities can immediately be noticed, especially in the 20-50 Hz frequency range. In particular, at 20 Hz LIGO Livingston's ASD is almost two times lower than LIGO Hanford's ASD.

We acknowledge the fact that using the quicker model might influence the results we achieve and note that further investigation of this difference might be necessary in the future. It is also worth noting that the difference in strain between detectors is much more pronounced in the NRSur7dq4 model, and it further increases LIGO Livingston's expected higher SNR.

We later prepared further visualizations of the data. We plotted the whitened strain along with the maximum likelihood IMRPhenomXPHM waveforms resulting from full, Hanford-only and Livingston-only PE in Figure 3. There is only a slight difference between the LIGO Livingston-only estimated waveform and estimated waveform using both detectors, which can be expected considering that the two-detectors inference is driven by LIGO Livingston due to LIGO Livingston's higher SNR. We see, however, significant differences between the waveform resulting from LIGO Hanford-only PE and the other two runs. In particular, there is significant discrepancy between the calculated waveform and LIGO-Livingston strain data observed in the inspiral phase.

4.2. *Comparing PE results*

We present partial PE results for the main compact binary coalescence parameters from LIGO Hanford-only and LIGO Livingston-only data in Figure 4. We also present pairwise Jensen-Shannon divergences for the three PE runs in Table 1. The estimated values from PE with 90% confidence intervals are shown in Table 2.

Those results by themselves are very interesting. The median masses differ noticeably (total mass values of $M^{\rm H} = 330^{+36}_{-55}\ M_\odot$ vs. $M^{\rm L} = 286^{+20}_{-26}\ M_\odot$), but the differences in luminosity distance (and inclination, which is coupled with it) and spins are the most striking. LIGO Hanford-only data favor medium values of $\chi^{\rm H}_{\rm eff} = 0.48^{+0.23}_{-0.50}$ and $\chi^{\rm H}_{\rm p} = 0.45^{+0.35}_{-0.26}$, while the LIGO Livingston-only data favor low $\chi^{\rm L}_{\rm eff} = 0.03^{+0.15}_{-0.22}$ and very significant precession with $\chi^{\rm H}_{\rm p} = 0.72^{+0.21}_{-0.23}$. Typically, the luminosity distance and the inclination can be degenerate, but this degeneracy can be lifted in precessing systems (Usman et al. 2019) – such as GW231123 if $\chi_{\rm p}$ really has such an extreme value. Using Hanford data results in $\iota^{\rm H} = 1.53^{+1.35}_{-1.27}$ and $D^{\rm H}_{\rm L} = 4064^{+2905}_{-2758}$ Mpc, while Livingston data constrains those much better at $\iota^{\rm L} = 1.47^{+0.69}_{-0.55}$ $D^{\rm L}_{\rm L} = 568^{+390}_{-271}$ Mpc. We consider these differences significant and we believe their further investigation is warranted.

Table 1. Jensen–Shannon divergences of selected parameters between detector combinations.

Parameter	L1 vs. H1	H1 vs. H1L1	L1 vs. H1L1
redshift z	0.6093	0.5831	0.1916
luminosity distance $D_{\rm L}$	0.609	0.584	0.191
$\theta_{\rm JN}$	0.498	0.523	0.011
$\chi_{\rm eff}$	0.477	0.463	0.005
phase	0.467	0.430	0.015
primary mass	0.376	0.394	0.006
total mass M	0.373	0.369	0.009
inclination ι	0.352	0.312	0.008
$\chi_{\rm p}$	0.236	0.263	0.003
secondary mass	0.098	0.137	0.014
χ_1	0.020	0.014	0.008
χ_2	0.003	0.010	0.018

4.3. *Low frequency part of the spectrum*

We have also ran PE on data from both detectors in a different frequency range of 10-256 Hz instead of the standard 20-256 Hz. Typically including data from this low frequency region doesn't improve the fit because of significant noise. It could, however, be theorized that including this part of the spectrum is helpful in GW231123's case, as it is a significantly more massive event and therefore is detected at lower frequencies, so we reran the analysis on the 10-256 Hz frequency range. Afterwards we concluded that changing the lower limit of frequency didn't impact the posterior distributions in a way that would be distinguishable from random seed change in different PE runs, therefore we will not include the lower frequency range in our further analysis.

5. INJECTION STUDY

We have prepared an injection study setup based on numerical relativity waveforms for a system similar to GW231123. The first waveform we'll examine is SXS050 (Scheel et al. 2025), a binary black hole coalescence of two black holes with equal masses of 150

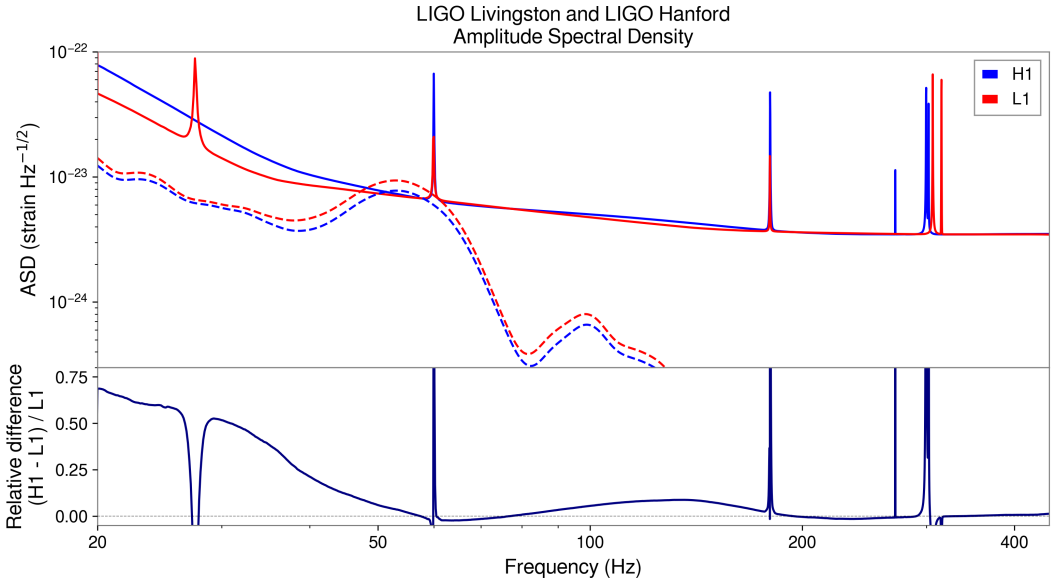

Figure 1. Top plot: ASD of LIGO Livingston (red), LIGO Hanford (blue) and of the average waveform resulting from NRSUR7DQ4 PE posterior samples for both of the interferometers (average waveform resulting from LIGO Hanford+LIGO Livingston PE posteriors). Bottom plot: relative difference in ASD of the two interferometers defined as $(\mathrm{ASD}_{\mathrm{H}_1} - \mathrm{ASD}_{\mathrm{L}_1})/\mathrm{ASD}_{\mathrm{L}_1}$.

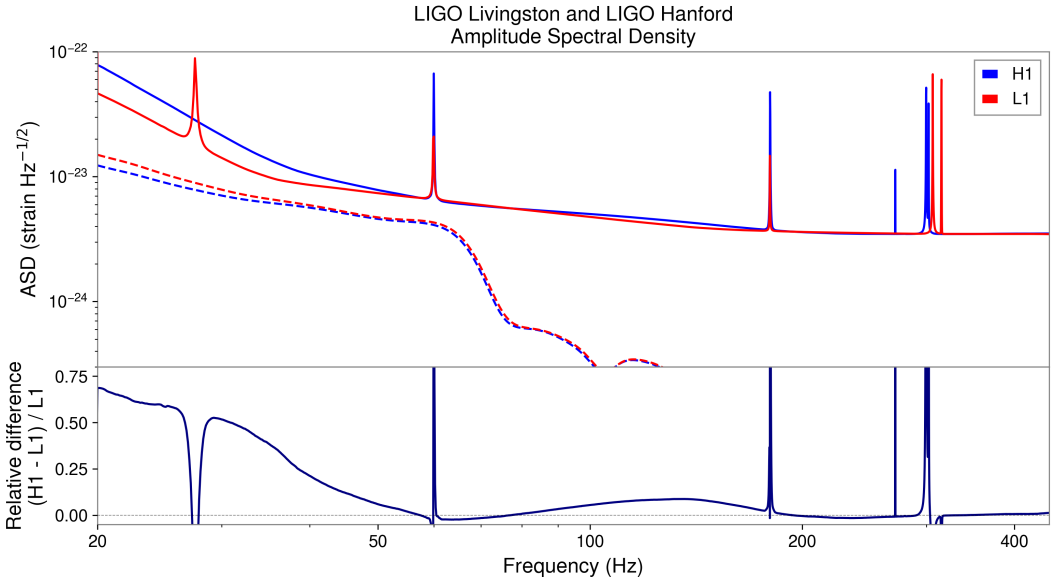

Figure 2. Top plot: ASD of LIGO Livingston (red), LIGO Hanford (blue) and of the average waveform resulting from IMRPHENOMXPHM PE posterior samples for both of the interferometers (average waveform resulting from LIGO Hanford+LIGO Livingston PE posteriors). Bottom plot: relative difference in ASD of the two interferometers defined as $(\mathrm{ASD}_{\mathrm{H}_1} - \mathrm{ASD}_{\mathrm{L}_1})/\mathrm{ASD}_{\mathrm{L}_1}$.

$M_\odot$, $\chi_{\mathrm{eff}} = 0.159$ and $\chi_{\mathrm{p}} = 0.940$ at luminosty distance $D_{\mathrm{L}} = 4043$ Mpc and $\iota = 0.88$. Examining the numerical relativity result will ensure we use realistic, high-fidelity waveforms without introducing errors associated with other waveform approximants; it does, however, severely limit the parameter space that can be explored as there exists a limited number of those solutions.

We will inject SXS050 signal into different Gaussian noise realizations using the same PSD as for GW231123, and infer the properties of the injected signal as described in Section 3, separately for LIGO Hanford and LIGO Livingston. We will evaluate whether the same level of discrepancies that was observed for GW231123 will also be observed for these injections.

Table 2. Posterior values of selected parameters from 3 PE runs for GW231123 with 90% confidence intervals. Masses are given in source's frame of reference.

Parameter	H1	L1	H1+L1
luminosity distance $D_{\rm L}$ (Mpc)	4064^{+2905}_{-2758}	568^{+390}_{-271}	851^{+349}_{-293}
redshift z	$0.658^{+0.363}_{-0.407}$	$0.118^{+0.072}_{-0.054}$	$0.171^{+0.062}_{-0.055}$
χ_1	$0.79^{+0.18}_{-0.40}$	$0.75^{+0.20}_{-0.26}$	$0.79^{+0.18}_{-0.26}$
χ_2	$0.60^{+0.36}_{-0.53}$	$0.54^{+0.40}_{-0.48}$	$0.68^{+0.28}_{-0.55}$
$\chi_{\rm eff}$	$0.48^{+0.23}_{-0.50}$	$0.03^{+0.15}_{-0.22}$	$0.05^{+0.16}_{-0.21}$
$\chi_{\rm P}$	$0.45^{+0.35}_{-0.26}$	$0.72^{+0.21}_{-0.23}$	$0.74^{+0.19}_{-0.24}$
inclination ι (rad)	$1.53^{+1.35}_{-1.27}$	$1.47^{+0.69}_{-0.55}$	$1.41^{+0.80}_{-0.56}$
log likelihood	$90.2^{+3.0}_{-4.6}$	$149.4^{+3.7}_{-5.0}$	$244.9^{+3.7}_{-5.4}$
primary mass ($M_\odot$)	128^{+38}_{-31}	157^{+14}_{-13}	150^{+13}_{-12}
secondary mass ($M_\odot$)	69^{+31}_{-26}	98^{+22}_{-27}	94^{+19}_{-20}
total mass ($M_\odot$)	330^{+36}_{-55}	286^{+20}_{-26}	285^{+21}_{-21}
mass ratio	$0.55^{+0.35}_{-0.28}$	$0.62^{+0.15}_{-0.17}$	$0.63^{+0.12}_{-0.13}$
geocentric time since 1384782888 (s)	$0.6018^{+0.0240}_{-0.0217}$	$0.6020^{+0.0258}_{-0.0166}$	$0.6268^{+0.0026}_{-0.0035}$
phase (rad)	$2.89^{+2.57}_{-2.10}$	$5.10^{+0.43}_{-0.50}$	$5.03^{+0.60}_{-0.58}$
$\theta_{\rm JN}$ (rad)	$1.56^{+1.33}_{-1.30}$	$1.56^{+0.46}_{-0.40}$	$1.54^{+0.41}_{-0.37}$

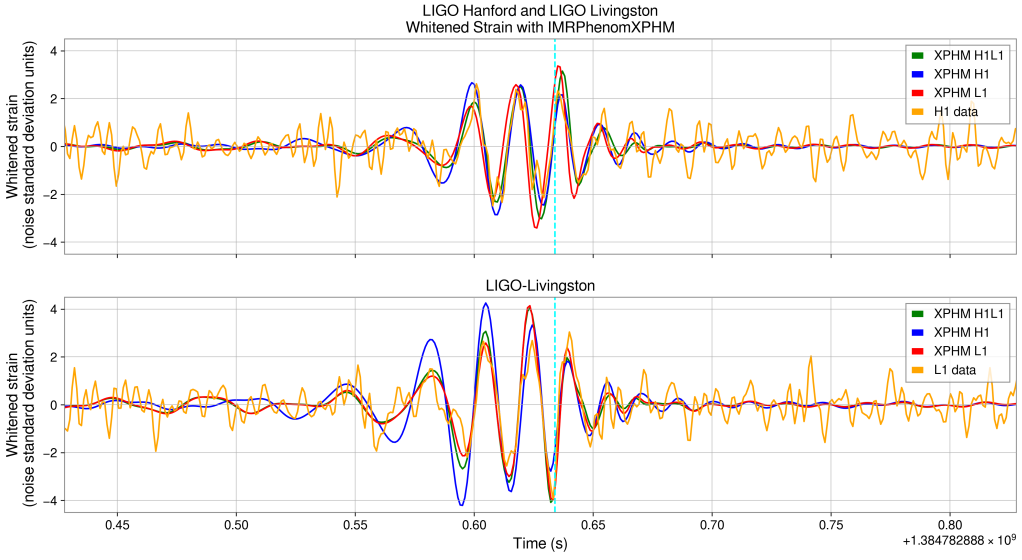

Figure 3. Whitened strain bandpassed to the frequency range [20Hz, 256Hz] (orange) plotted with best fitting IMRPhenomXPHM waveform models from LIGO Hanford+LIGO Livingston (green), LIGO Hanford-only (blue) and LIGO Livingston-only (red) PE for both LIGO interferometers. The y-axis is in noise standard deviation units.

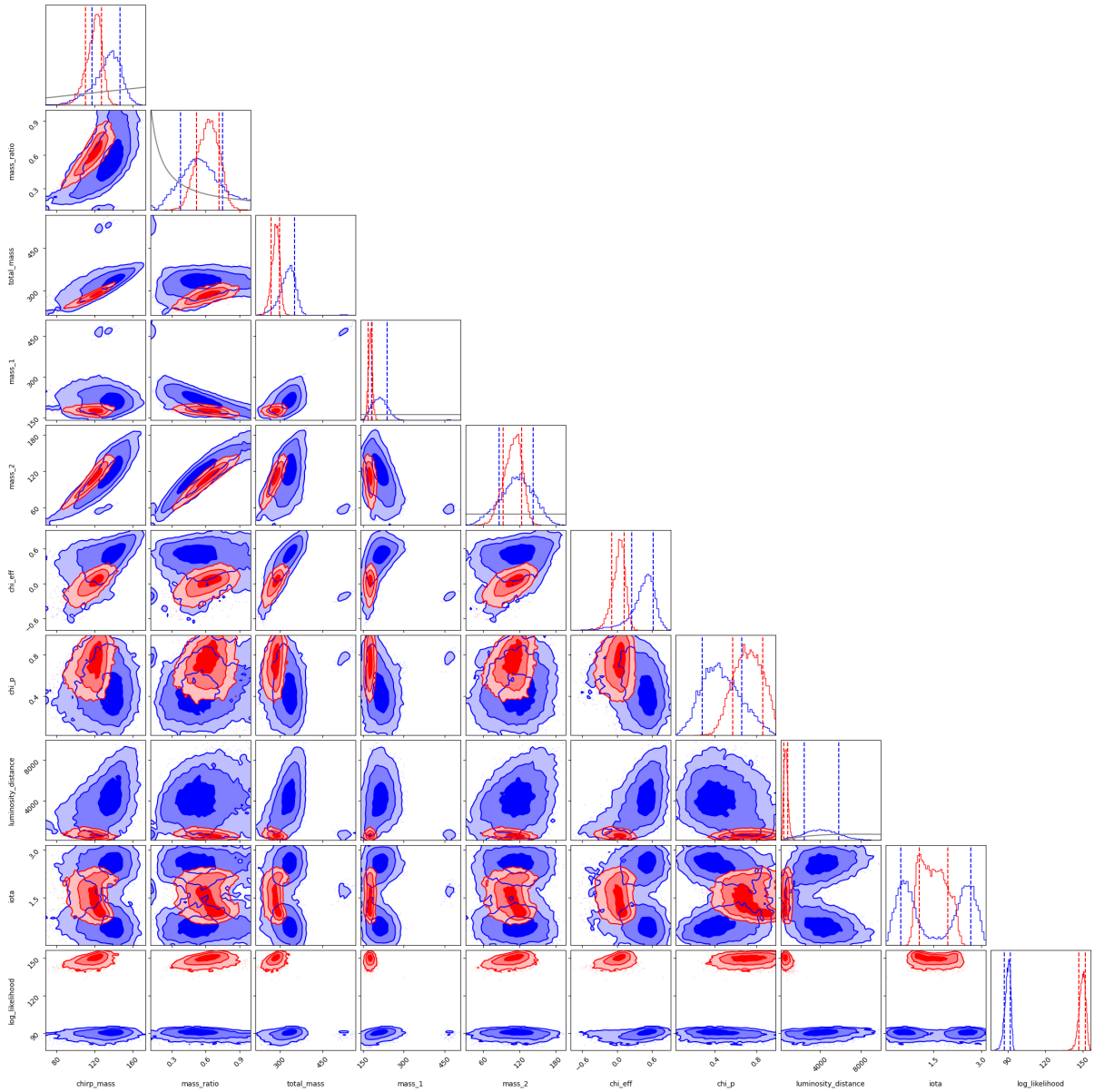

Figure 4. Comparison of LIGO Hanford-only (blue) and LIGO Livingston-only (red) parameter estimation results. Gray line on histograms indicates prior.

REFERENCES

Abbott, R., et al. 2020a, PhRvL, 125, 101102, doi: 10.1103/PhysRevLett.125.101102

—. 2020b, ApJL, 900, L13, doi: 10.3847/2041-8213/aba493

Ashton, G., Hübner, M., Lasky, P. D., et al. 2019, ApJS, 241, 27, doi: 10.3847/1538-4365/ab06fc

Blanchet, L. 2014, Living Reviews in Relativity, 17, 2, doi: 10.12942/lrr-2014-2

Chatziioannou, K., Cornish, N., Wijngaarden, M., & Littenberg, T. B. 2021, Phys. Rev. D, 103, 044013, doi: 10.1103/PhysRevD.103.044013

Christensen, N., & Meyer, R. 2022, Reviews of Modern Physics, 94, 025001, doi: 10.1103/RevModPhys.94.025001

Cornish, N. J., & Littenberg, T. B. 2015, Class. Quant. Grav., 32, 135012, doi: 10.1088/0264-9381/32/13/135012

Cornish, N. J., Littenberg, T. B., Bécsy, B., et al. 2021, Phys. Rev. D, 103, 044006, doi: 10.1103/PhysRevD.103.044006

Farmer, R., Renzo, M., de Mink, S. E., Marchant, P., & Justham, S. 2019, ApJ, 887, 53, doi: 10.3847/1538-4357/ab518b

Ng, K. K. Y., Vitale, S., Zimmerman, A., et al. 2018, PhRvD, 98, 083007, doi: 10.1103/PhysRevD.98.083007

Pratten, G., García-Quirós, C., Colleoni, M., et al. 2021, PhRvD, 103, 104056, doi: 10.1103/PhysRevD.103.104056

Racine, É. 2008, PhRvD, 78, 044021, doi: 10.1103/PhysRevD.78.044021

Scheel, M. A., Boyle, M., Mitman, K., et al. 2025, arXiv e-prints, arXiv:2505.13378, doi: 10.48550/arXiv.2505.13378

Thomas, L. M., Schmidt, P., & Pratten, G. 2021, Phys. Rev. D, 103, 083022, doi: 10.1103/PhysRevD.103.083022

Usman, S. A., Mills, J. C., & Fairhurst, S. 2019, ApJ, 877, 82, doi: 10.3847/1538-4357/ab0b3e

Varma, V., Field, S. E., Scheel, M. A., et al. 2019, Phys. Rev. Research., 1, 033015, doi: 10.1103/PhysRevResearch.1.033015